AIAA JOURNAL
Vol. 39, No. 6, June 2001

Inferring Propeller Inflow and Radiation from Near-Field Response, Part 2: Empirical Application

R. J. Minniti* and W. K. Blake†
U.S. Naval Surface Warfare Center, West Bethesda, Maryland 20817-5700
and
T. J. Mueller‡
University of Notre Dame, Notre Dame, Indiana 46556

Data analysis techniques were previously developed for rotating machinery that predicted the far-field radiation, inferred inflow characteristics, and defined the near-field/far-field acoustic Green's function based on measurements of the pressure near field (Minniti, R. J., Blake, W. K., and Mueller, T. J., "Inferring Propeller Inflow and Radiation from Near-Field Response, Part 1: Analytic Development," *AIAA Journal*, Vol. 39, No. 6, 2000, pp. 1030–1036). The techniques are applied to a free-running propeller in subsonic flow. As a first case, the propeller ingesting large-scale, mean-flow distortions as would be present downstream of stators or inlet guide vanes was considered. This simplified case allowed qualitative analysis in the time domain and complimenting quantitative analysis in the frequency domain. In addition, the case acted as a calibrating configuration to map the frequency response of the individual blades to the incoming flow by varying the number of distortions present and the rotational speed of the propeller. Based on the results of the first case, the analysis was extended to the propeller ingesting grid-generated turbulence. Because of the complex nature of the flow, all analysis was completed in the frequency domain. By the use of the techniques in "Inferring Propeller Inflow and Radiation from Near-Field Response, Part 1: Analytic Development," an estimate of the blade summation gain was used to complete the direct solution of the aeroacoustic problem and predict the acoustic far field from a measurement of the ingested flow. Additionally, the inflow character was inferred from the near-field measurements.

Nomenclature

B	=	blade number
c	=	airfoil chord
c_0	=	speed of sound
f	=	frequency in cycles
J	=	advance ratio, $U_\infty / n_s D$
K	=	calibration function
k_1^*	=	primary reduced frequency, $\omega c / 2U_\infty$
M	=	characteristic mesh size
M_∞	=	freestream Mach number, U_∞ / c_0
n_s	=	rotational speed of propeller, revolutions per second
p	=	unsteady pressure on airfoil
$Se(k_1^*)$	=	Sears function
t	=	time
U_∞	=	freestream velocity
u	=	unsteady velocity
$\boldsymbol{x}$	=	blade position vector
ρ	=	density of air
Φ_x	=	two-sided auto-spectral density
Ω	=	propeller shaft rate
ω	=	circular frequency

Subscripts

i	=	quantities associated with individual blades
Σ	=	quantities associated with sum of ring array
1	=	chordwise, scalar component of a vector
2	=	normal, scalar component of a vector
3	=	spanwise, scalar component of a vector

Superscript

$*$	=	quantity normalized by half chord

Introduction: Problem Statement

UNDERSTANDING the response of rotating machinery to the ingestion of unsteady flow in a manner that has practical application to identification and removal of specific noise sources is complicated by many factors. The most significant of these are the lack of experimental methods appropriate to characterize the propeller response and the inability of existing model results to scale to full-scale application. The total propeller response typically must be inferred from a comparison of the measured acoustic radiation and the calculated individual blade response. The individual blade response is a result of local interaction with the flow whereas the total response is due to global interaction of the propeller with the ingested flowfield. Effectively, the propeller geometry samples the flow at many circumferentially periodic locations creating near-field pressure responses around each sampling blade. In the near field of the propeller, the fluid acts as a summing medium, suppressing some blade response characteristics while emphasizing others based on the local correlation of pressure. Therefore, the total response and ultimately the acoustic radiation of the propeller in unsteady flow result from a complex interaction of the flow characteristics and propeller geometry.

In Ref. 1, techniques were presented to use experimental data obtained upstream of the propeller, at the surface of propeller blades and in the acoustic far field to characterize this complex response. The techniques take advantage of the circumferentially periodic propeller geometry and use the blade positions as optimal measurement locations for determining the total response. Thus, interpretation of the near-field pressure data was reduced to intuitive assumptions about how the fluid summed the individual contributions of the blades. The primary objective of the research was to characterize unsteady thrust production. If the fluid response to thrust can be approximated by a linear summation of individual blade response, the sum of the blade surface pressures can be used to characterize the total thrust response. Therefore, motivation is given for using direct measurements of the pressure near field to predict the acoustic response of the propeller in unsteady flow.

Received 20 July 1999; revision received 20 November 2000; accepted for publication 4 December 2000.

*Mechanical Engineer, Signatures Directorate, Carderock Division.
†Chief Research Scientist, Signatures Directorate, Carderock Division.
‡Roth-Gibson Professor, Department of Aerospace and Mechanical Engineering. Associate Fellow AIAA.

The strategy for using the near-field data was applied to a free running propeller ingesting unsteady flow. The instrumentation scheme was chosen to give all of the data necessary to apply the method. Additionally, the flowfields were designed to bring out aspects of the acoustic response that would be clearly demonstrated by the method. Thus, the use of large-scale, mean-flow distortions, such as are present downstream of stators or inlet guide vanes, were analyzed first. These types of flows represent validation cases for the methods and calibrating cases for empirically describing the individual blade response to the incoming flow. With such a description, it is not necessary to rely on an analytic development of the response of the real blade geometry. The technique was then applied to the propeller operating in grid-generated turbulence extending the use of the methods.

In practical applications, the flow ingested by rotating machinery is typically a combination of both types of flows. Therefore, because the method is robust in both cases, it can be used as an in situ measurement scheme for direct identification and removal of ingested noise sources. Note that the techniques do not describe other noise sources such as Gutin noise, trailing-edge noise, or other forms of noise not associated with the leading-edge reaction of the blade to the incoming flow. Finally, the development in Ref. 1 was appropriate for propellers operating in subsonic flow, that is, $M_\infty < 0.15$.

Experimental Approach

The experiment consisted of an instrumented four-blade model propeller ingesting large-scale and small-scale nonuniform flowfields in an anechoic wind tunnel. The Anechoic Wind Tunnel at the University of Notre Dame is described by Mueller et al.[2,3] To summarize, the facility is a 0.61×0.61 m (2×2 ft) freejet wind tunnel capable of freestream flow speeds of 33 m/s (108 ft/s). The tunnel is enclosed in an anechoic chamber 9.14 m (30 ft) long by 7.35 m (24 ft) wide by 3.66 m (12 ft) high. The jet produces quiet, laminar flow with a mean turbulence intensity of less than 0.1% along the centerline. Acoustic treatments on the walls, ceiling, and floor, coupled with mufflers on the diffuser, create an ambient noise at 1000 Hz of 30-dB Re 20 μPa at 0.91 m (3 ft) from the jet centerline for a flow speed of 17 m/s (56 ft/s). The low-frequency cutoff of the chamber is less than 100 Hz. The use of this facility allows measurements to be made of the incoming flowfield, the near-field pressure response of the propeller blades, and the far-field direct radiation of the propeller operating in unsteady flow.

A microphone boom is mounted on the ceiling of the chamber allowing automated and repeatable positioning of microphones within the anechoic region of the tunnel. The motion of the boom allows multiple measurements of the sound field along an arc in the acoustic field. Minniti et al.[4] estimated the uncertainty in sound pressure level (SPL) measurement to be ± 0.8 dB Re 20 μPa. Typically, the SPL in the chamber is measured using a B&K 1.27-cm (0.5-in.) Type-4181 or a 6.35-cm (0.25-in.) Type-4135 microphone with acoustic sensitivity of approximately 87 or 43 mV/Pa, respectively. The microphones are calibrated before each experiment using a B&K pistonphone (Type 4228) and calibration barometer (Type UZ0004).

The facility has an automated traverse for making hot-wire or hot-film measurements of the flow. Both single-wire and cross-wire measurements are typical and the methods of calibration and assessment of measurement uncertainty have been addressed by Scharpf[5] and Minniti.[6] Generally stated, the uncertainty of single-wire measurements is $\pm 1\%$ of mean-flow values and $\pm 2\%$ of turbulent levels. For cross-wire measurements, the uncertainty is much more difficult to assess analytically. However, based on end-to-end measurements and the estimated bias error, the uncertainty in the turbulent component is given as $\pm 5\%$ of the reported value. In addition to measurements taken using the automated traverse, a hot wire was mounted on one of the propeller blades to sample the flow just forward of the blade leading edge during some of the experiments.

The propeller was a left-hand, four-blade propeller (Model 3174) with a diameter of 25.4 cm (10 in.). Made originally at the David Taylor Model Basin as part of a larger study, it was selected for the current research due to its availability and simple geometry. The propeller has thin blade sections resembling 3% thick NACA airfoils with chord of approximately 5.1 cm (2 in.) at the 70% span.

Table 1 Location of PVDF pressure transducers on propeller

Sensor number	Radial location $x_3/L_3 \times 100\%$	Chordwise location $x_1/c \times 100\%$	Sensor description
1–4	70	8.9	Ring, SS
5	82.5	7.3	Tip, SS
6	65	9.4	Midspan, SS
7	57.5	9.6	Hub, SS
8	82.5	7.3	Tip, PS
9	65	9.4	Midspan, PS

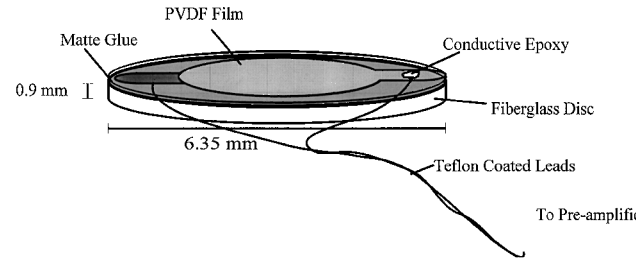

Fig. 1 Sensor construction.

The blades have small leading- and trailing-edge skew so that the overall blade planform has little skew or rake. The propeller pitch is 32.1 cm (12.62 in.) at the 70% span and the expanded area ratio is 0.45. The design advance ratio of the propeller is roughly 1.2, and the zero thrust advance ratio is 1.4.

The propeller was instrumented with small polyvinylidine fluoride (PVDF), unsteady-pressure transducers on each blade. As shown in Fig. 1, the transducers were constructed of a small section of PVDF film mounted on a stiff fiberglass wafer. The film/wafer combination was then mounted flush to the blade surface with soft cure silicon to provide mechanical isolation between the blade and sensor. The PVDF signal was carried by a twisted pair of wires to the hub of the propeller, where its high impedance output was amplified by the circuitry shown in Fig. 2. This low impedance signal was then brought to the stationary reference frame with water-cooled, mercury slip rings.

Once installed in the propeller, the sensors were calibrated for both phase and magnitude response relative to a B&K 6.35-cm (0.25-in.) Type-4135 microphone. Calibration involved exposing both transducers to a combination of white noise and swept sine waves broadcast through a loud speaker in the anechoic chamber. To assure accurate characterization of PVDF response over a wide range of frequencies, the two transducers were placed as close to each other as possible with the speaker placed at a large distance. Additionally, calibration data obtained when the coherence between the two sensors was less than 0.95 was rejected. The complete response function was, therefore, obtained during a series of calibration experiments with varying levels of amplitude and frequency content. The frequency-response phase and magnitude found during a typical calibration experiment is shown in Fig. 3. The sensor calibration procedure and the results of previous experiments to measure unsteady pressure on the surface of thin airfoils and model propellers in unsteady flow are described by Minniti et al.,[7] Minniti and Mueller,[8] and Lynch et al.[9] In Ref. 10, the uncertainty of the transducers was estimated to be $\pm 8\%$ of the reported value.

Strategy for Propeller Instrumentation

The four-blade propeller instrumented with sensors on each blade is shown in Fig. 4a. In a typical experiment, the instrumented propeller is placed in a distorted flowfield as in Figure 4b. Ideally, an array of sensors that sampled the unsteady pressure at many points on each propeller blade would have enabled complete characterization of the unsteady lift. Because this was not possible, a smaller number of sensors were arranged on the propeller such that they produced three transducer arrays with acoustically relevant spatial distributions. In particular, the arrays assessed the blade-to-blade correlation of unsteady blade lift, the spanwise correlation of the

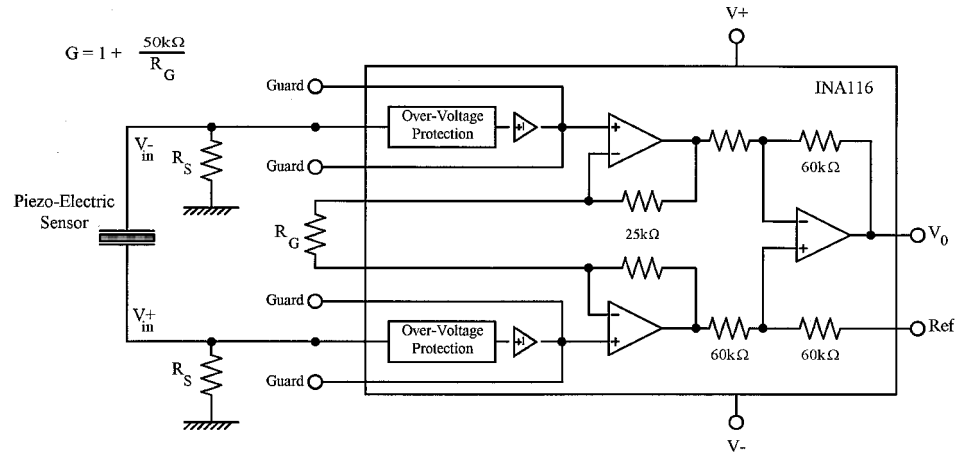

Fig. 2 Schematic of preamplification circuitry installed in propeller hub.

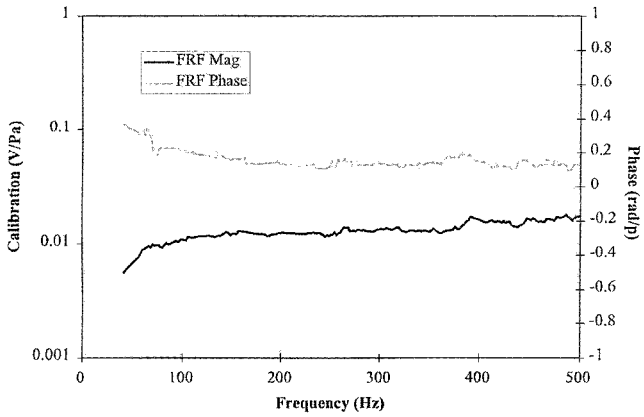

Fig. 3 Typical PVDF transducer frequency-response function obtained during calibration experiment. (Note: sensitivity scale is logarithmic on left and phase scale is linear on right.)

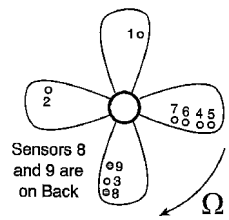

Fig. 4a Instrumented propeller.

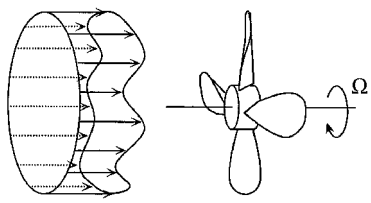

Fig. 4b Propeller operating in unsteady flow.

unsteady lift, and the antisymmetry of unsteady pressure jump. Each of these helps to characterize the global propeller response to the unsteady flowfield as outlined in Ref. 1. Table 1 lists all sensor locations, where the pressure side (PS) and suction side (SS) of the blade are noted, respectively.

A ring of four sensors placed at a constant radial and chordwise location on the suction face of each blade made up the first array. The sensors were located at 10% of the chord and 70% of the span. The chordwise location was selected to sample the blade response near the leading edge, where the unsteady pressure due to the leading edge interaction would be greatest in magnitude. The radial location was chosen to place the sensor at the location that would best characterize the total blade response. Because the steady blade loading is greatest at approximately 70% of the span, the unsteady

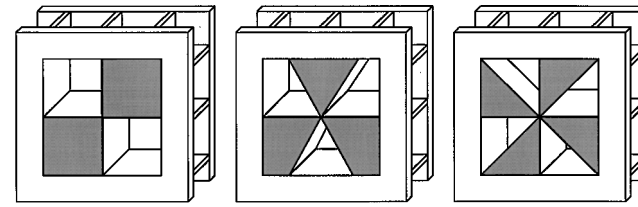

Fig. 5 Actual model propeller mounted on dynamometer in front of cyclic flow distortion screen.

lift was analogously anticipated to be greatest in this region due to increased rotational velocity and local blade chord. The single point measurement sampled the unsteady pressure at a point most representative of the individual blade response, and the array characterized the total propeller response. Thus, summations of the four sensor signals characterized the essential behavior of the total unsteady force by assuming a linear relationship existed between the single point unsteady pressure and the total unsteady blade lift.

On two of the blades, sensors were arranged in spanwise arrays. The first of these included the fourth sensor from the ring array and three other sensors, all located on the suction face of the blade. The four sensors were centered about 65% of the span giving a measure of the spanwise correlation of the unsteady pressure for several separation lengths. The last array included the third sensor from the ring array and two sensors placed on the pressure face of the same blade. These sensors allowed for an investigation of the antisymmetry of unsteady pressure jump as well as effects of flow separation. These effects were present on the suction face of the blades under mean loading conditions.

Unsteady/Nonuniform Flow Generators

The propeller was exposed to flows composed of both spatially nonuniform mean flow and turbulence. The flowfields fell generally into one of two categories. The first of these were large-scale, steady, nonuniform flows that were circumferentially periodic. The second class of flows involved grid generated turbulence with different characteristic eddy sizes produced by varying the mesh solidity and composition. The screens generated flows that produced specific levels of blade-to-blade correlation of unsteady pressure. Blade-to-blade correlation of unsteady pressure enhances unsteady thrust and side force production, the primary sources of acoustic radiation during the experiment. Therefore, by characterizing the types of propeller forces using the unsteady pressure arrays, estimates of the expected acoustic radiation were made for comparison to far-field measurements.

The cyclic devices, shown in Fig. 5, were designed such that the propeller ingested spatially harmonic, nearly sinusoidal, variations of the mean flow during rotation. Therefore, shaft-rate-multiple spectral modes characterized the flows, making analysis of the response more straightforward than broadband turbulence ingestion. These cyclic devices produced large-scale flow distortions of two,

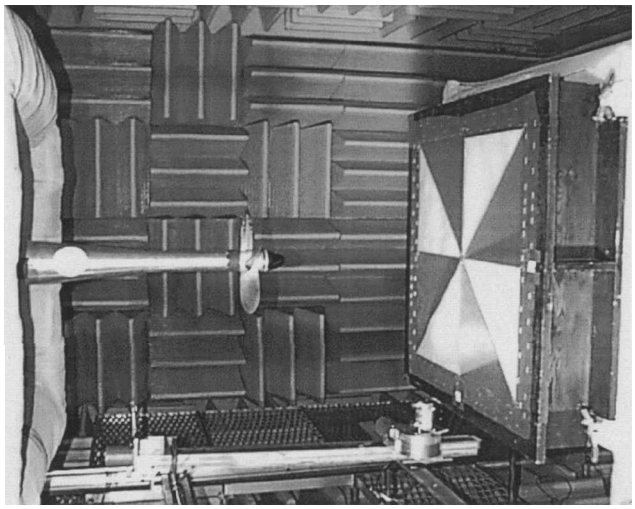

Fig. 6 Diagram of cyclic distortion devices used in experiments.

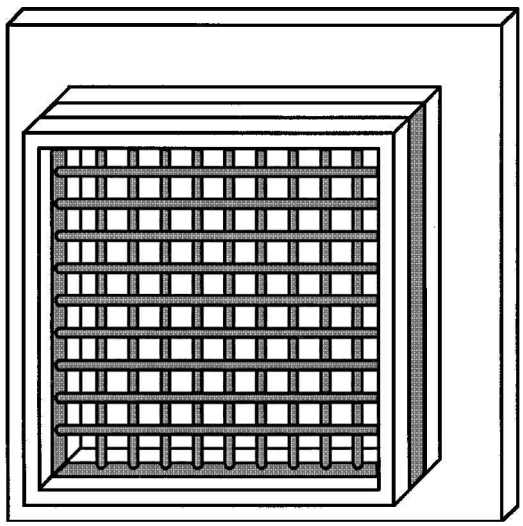

Fig. 7 Diagram of turbulence generating grid used in experiments.

three, and four cycles per shaft rotation. The magnitude, direction, and spectral character of the net propeller response were determined by these harmonic features. Subramanian and Mueller[11] carefully documented the circumferential and radial variation of the mean and turbulent flows produced by these screens at several axial stations in the flow. The analysis of the propeller response to these flows allowed for their use as known or calibrating flow conditions. Figure 6 shows a photograph of the instrumented propeller at its operating location in front of the four-cycle flow generator.

Figure 7 shows an example of the turbulence generating grids that were placed in the flow upstream of the propeller. A total of three grids were used during the experiments with characteristic mesh sizes of 1.9 (0.75), 3.2 (1.25), and 7.6 cm (3.0 in.). Turbulence intensity, correlation length, and spectral character of the turbulence are all related to the characteristic mesh size of the grids. As discussed in Ref. 1, the production of unsteady force on the rotating propeller is dependent on the length scale of the turbulence by two separate mechanisms. The first involves reduction of the individual blade lift by correlation lengths smaller than the blade span. The second is the blade-to-blade coupling produced by turbulent length scales on the order of the blade spacing. This coupling enhances unsteady force and is responsible for both tonal and broadband elevation of the radiated noise near the blade rate harmonics. Scharpf and Mueller[12] characterized propeller broadband radiation due to the grid-generated turbulence, laying the basis for the measurements. However, in the current experiments, the combination of velocity, pressure near-field, and acoustic far-field measurements combined to characterize fully the propeller response.

Propeller Response to Cyclic Flow Devices

The results of exposing the propeller to the cyclic flow devices are presented first. These present canonical cases where the mean flowfield can be described by single point measurements of the flow. Additionally, these cases explore the extremes of unsteady flow correlation in terms of the propeller geometry. First, the mean flow distortions have little radial phase variation and create unsteady flow in the rotating reference frame that is well correlated along the span of the blade. Second, the mean flows are composed of circumferential modes that can be associated with shaft rate harmonics in the rotating reference frame producing specific levels of blade-to-blade correlation of lift. To eliminate effects of mean blade loading and minimize viscous effects, the data were obtained with the propeller operating in the flows at the zero mean thrust condition ($J = 1.4$).

The correlation conditions that occur between blades are shown in Figs. 8a and 8b. The four-cycle flow produces unsteady lift that is in phase from blade to blade for the four-blade propeller. When this condition occurs, a significant amount of unsteady thrust and acoustic radiation is anticipated at the blade rate harmonics. Alternatively, the three-cycle flow case produces unsteady flow that, while being correlated from blade to blade, forces opposite blade pairs out of phase. Thus, the individual blade contributions to unsteady thrust are canceled, and only side forces are produced at the blade rate frequency. The anticipated acoustic radiation at the blade rate frequency is much lower. Thus, the two flows create demonstration cases for using the sum of the ring array of pressure transducers to approximate the blade summation gain and to identify the acoustically relevant blade loading components. In fact, they form the ideal cases where little variation in summation gain exists along the span of the blades and the single location estimate is an accurate approximation of the total summation gain.

Figure 9 shows time traces of the unsteady pressure produced with the propeller operating at $J = 1.4$ (3000 rpm) downstream of the four-cycle distortion. The pressure signals are compared to the velocity measurement made by the rotating blade mounted hot wire. In Fig. 9, an arbitrary gain has been applied to the velocity data; as

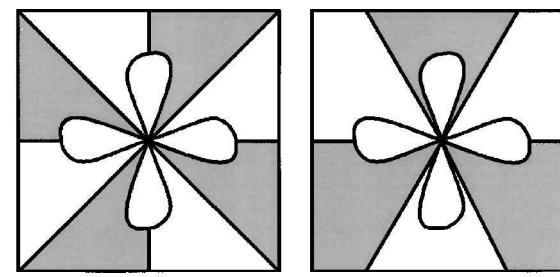

Fig. 8 Four-blade propeller operating downstream of four- and three-cycle distortions showing the generation of unsteady thrust and side forces.

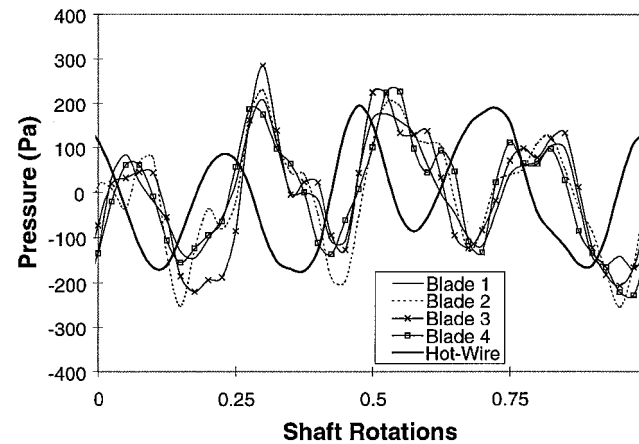

Fig. 9 Unsteady pressures measured on rotating propeller blades operating at $J = 1.4$ downstream of the four-cycle distortions.

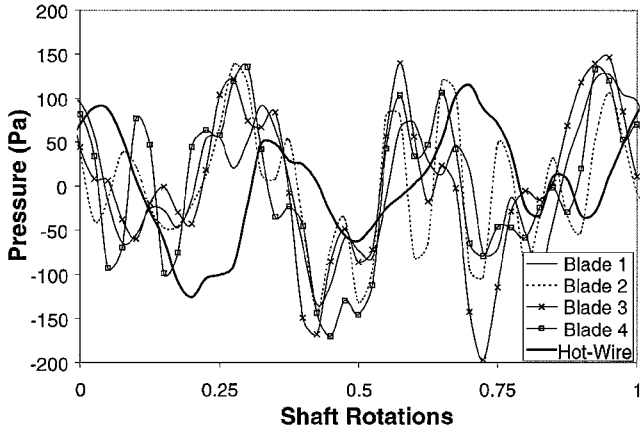

Fig. 10 Unsteady pressures measured on rotating propeller blades operating at $J = 1.4$ downstream of the three-cycle distortions.

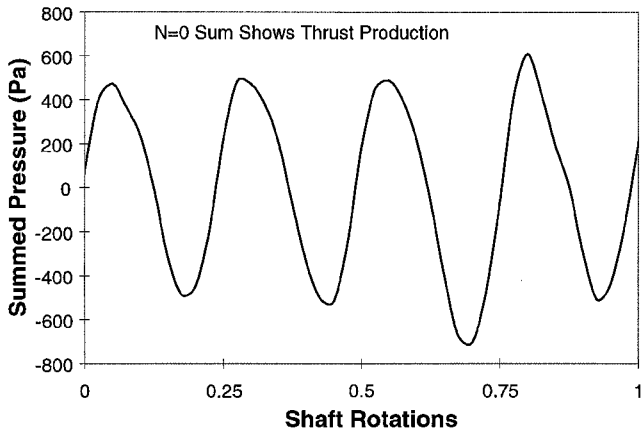

Fig. 11 Coherent sum of pressures measured on the blade of the propeller operating downstream of the four-cycle distortion at $J = 1.4$ large blade rate thrust.

such, the units have no quantitative meaning. The unsteady pressure and velocity have four distinct cycles within the shaft rotation. Thus, the pressure distortions of all blades are in phase and produce a summation gain near B^2. In addition, the velocity and pressure measurements were made such that a phase shift between the two measurements of approximately π is expected. The observed phase shift is not exactly π because the unsteady lift coefficient contains an additional complex phase. This complex phase will be quantitatively examined by comparison to the phase predicted by the Sears function (Ref. 1) for the broadband turbulence case.

Figure 10 shows a similar plot for the propeller operating at $J = 1.4$ (3000 rpm) downstream of the three-cycle distortion screen. The signals from each of the sensors have been shifted by a quarter shaft rotation to account for tangential location of the blades. When the signals are shifted in Fig. 10, the presence of the three-cycle distortion produced by the screen is clearly shown. Additionally, the shift demonstrates how the spatial filter associated with the side-force summation gain predicts blade rate side force. However, the shifting obscures the importance of the relative phase between sensor signals in the rotating frame. If the signals are not phase shifted, then the opposing pairs of sensors, that is, sensors 1 and 3 and sensors 2 and 4, are π out of phase with each other. Thus, when summed, no thrust is produced, which indicates the axial summation gain is zero.

Figures 11 and 12 show the results of summing the unsteady pressure data from Figs. 9 and 10 in the time domain. This summation was defined in Ref. 1 as

$$p_{\Sigma}^{0}(t) = \sum_{j=1}^{B} p_j(t) \tag{1}$$

In the preceding figures (i.e., Figs. 9 and 10), the unsteady pressure fluctuated between −150 and 150 Pa. However, in Figure 11 the

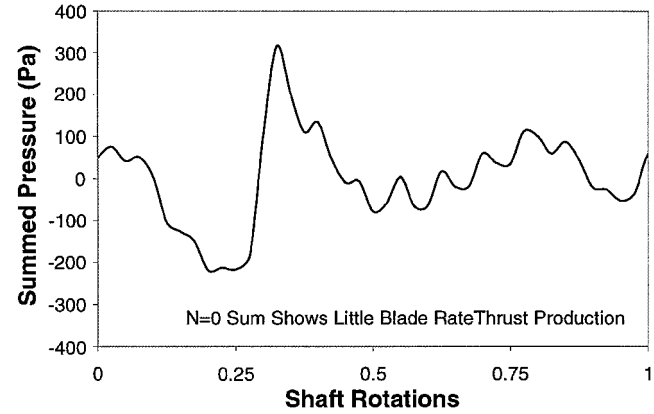

Fig. 12 Coherent sum of pressures measured on the blade of the propeller operating downstream of the three-cycle distortion at $J = 1.4$ showing little blade rate thrust.

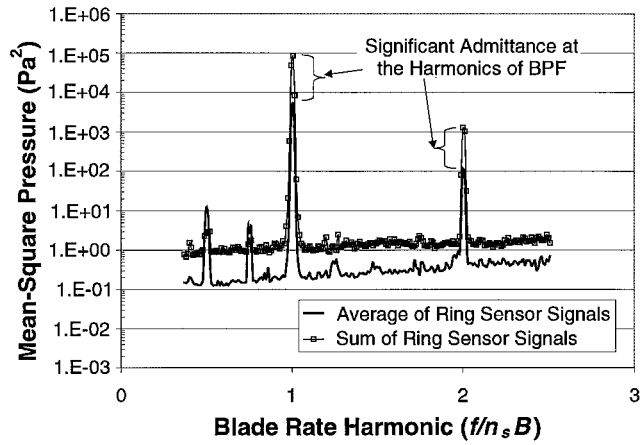

Fig. 13 Spectral decomposition of unsteady pressures measured on the blades of the propeller operating at $J = 1.4$ downstream of the four-cycle distortion showing increased force at blade rate harmonics.

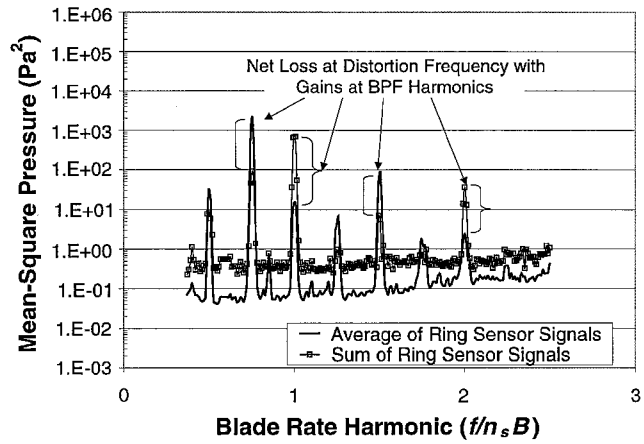

Fig. 14 Spectral decomposition of unsteady pressures measured on the blades of the propeller operating at $J = 1.4$ downstream of the three-cycle distortion showing increased force at the blade rate harmonics and a net loss at the distortion harmonics.

summed signal downstream of the four-cycle distortion fluctuates between −600 and 600 Pa. This indicates the amplitude of the four-cycle response was amplified by a factor of B, indicating the mean-square value increased by B^2. In contrast, Fig. 12 shows the summation nearly eliminated any fluctuation associated with the three-cycle mode. All that remains of the signal is a small one-cycle fluctuation that resulted from asymmetry in one of the cyclic screen distortion sections.

Figures 13 and 14 contain the summed signals in the frequency domain. In Figs. 13 and 14, the incoherently averaged pressure

spectrum of the array is compared to the spectrum of the coherent sum of the array signals. Figure 13 shows the amplification produced by summing the individual contributions downstream of the four-cycle distortion. At the harmonics of the blade passage frequency (BPF), which is coincident with the four-cycle distortion mode, the amplification is large. Other modes associated with harmonics of the shaft rate are significantly attenuated by the summing process. Alternatively, Fig. 14 shows the result downstream of the three-cycle device. For this case, the thrust summation reduced the levels at the distortion mode of three times the shaft rate. In fact, although this mode dominated the spectrum of the individual blade, the sum is dominated by the mode associated with blade passage. This result reflects the known feature that, while the propeller encounters a three-cycle distortion, the distortion/blade mismatch will not produce unsteady thrust. Therefore, in both cases, the only radiation above the broadband expected is at the blade rate harmonics.

Figures 15 and 16 show the results of using the spatial filtering definition of the side-force summation gain on the time data. This spatial filter was defined in Ref. 1 as

$$p_{\Sigma}^{1}(t) = \sum_{j=1}^{B} p_j(t) e^{[i(\theta_j + \Omega t)]} \tag{2}$$

where the blade indices θ_j are chosen to produce real and imaginary components of the sum corresponding to the horizontal and vertical components of force, respectively. In the four-cycle case, the spatial filtering has destructively summed the individual blade signals, indicating no production of side forces. However, in Fig. 16, the three-cycle case has produced significant fluctuations with four cycles per revolution. The real and imaginary signals are roughly

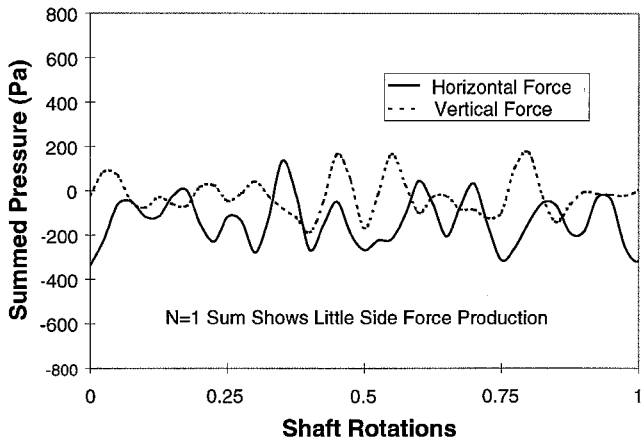

Fig. 15 Indexed sum of pressures measured on the blades of the propeller operating at $J = 1.4$ downstream of the four-cycle distortion showing no production of unsteady side force.

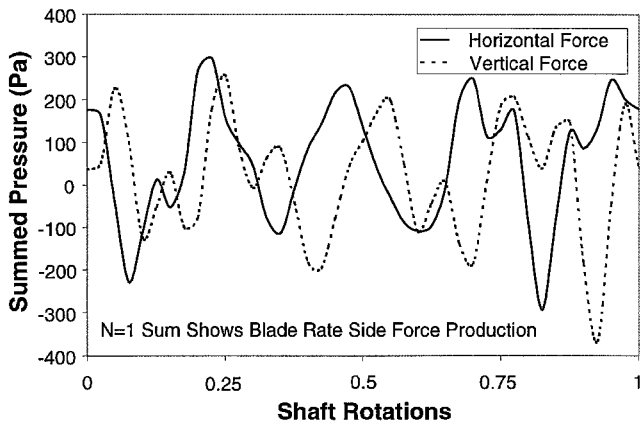

Fig. 16 Indexed sum of pressures measured on the blades of the propeller operating at $J = 1.4$ downstream of the three-cycle distortion showing production of unsteady side force.

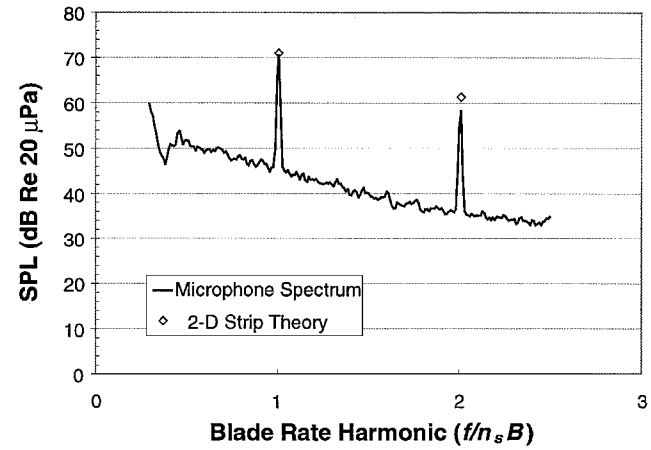

Fig. 17 Comparison of measured acoustic spectrum for the propeller operating at $J = 1.4$ downstream of the four-cycle distortion and the unsteady thrust dipole radiation predicted using two-dimensional strip theory approximation.

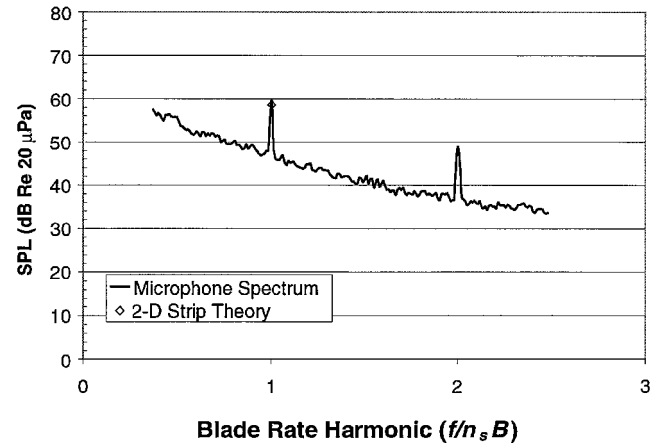

Fig. 18 Comparison of measured acoustic spectrum for the propeller operating at $J = 1.4$ downstream of the three cycle distortion and the unsteady side force dipole radiation predicted using two-dimensional strip theory approximation.

equal in magnitude, indicating a split of the side-force energy between the horizontal and vertical directions. This example shows how the transfer from the rotating frame to the stationary frame alters individual blade response at the distortion frequency, originally one shaft rate away from the BPF, into a propeller side force at the BPF.

Figures 17 and 18 show the SPL for the two cases. In Fig. 17, the radiation for the four-cycle case shows larger peaks at the BPF and harmonics. In Fig. 18, the three-cycle SPL spectrum shows smaller peaks at the BPF and harmonics with no peak at the original distortion frequency of three times the shaft rate. In each case, a prediction of the blade rate radiation has been made using the measured mean flow variation and the two-dimensional strip theory outlined in Ref. 1. For this case, the strip theory integration is greatly simplified because the unsteady flow is correlated along the entire span of the propeller blades. For the four-cycle flow case, the radiation results from an unsteady thrust dipole oriented axially in the flow. For the three-cycle case, the radiation is due to a side-force dipole oriented normal to the flow direction. For both cases, good agreement between the predicted peak level based on strip theory integration of lift and the measured peak is observed.

Propeller Response to Turbulence Ingestion

Although time-domain analysis for the cyclic flow cases demonstrated the effect of blade summation gain, its use in the case of general turbulence was impractical. Therefore, data from the propeller ingesting turbulence downstream of the 7.6-cm (3.0-in.) grid were treated only in the spectral domain. The treatment addressed

the pressure response of the individual blades as well as the complete solution of the direct aeroacoustic problem. First, the use of the two-dimensional, inviscid Sears function[1] on the lightly loaded propeller blade ($J = 1.2$) was tested by comparison of experimentally obtained velocity and pressure data. Second, based on the results of the preceding section, the empirical pressure response was mapped using data from the cyclic flow cases. Finally, from the velocity measurements and the empirically measured blade summation gain, the direct aeroacoustic problem was solved for the loaded propeller ($J = 1.2$) and compared to the measured acoustic radiation.

In Ref. 1, a general relationship between a sinusoidal gust and the resulting unsteady pressure response on a thin airfoil was given. The resulting expression,

$$\Delta p(x_1, \omega) = 2\rho u_2(\omega) U \sqrt{\left(1 - x_1^*\right)/\left(1 + x_1^*\right)}\, Se(\omega c/2U) \quad (3)$$

allowed analysis of the pressure response dependent on the chordwise extent of the unsteady flow structure. The primary focus was to express the relationship between the unsteady flow and the blade lift response. Therefore, this expression was integrated along the airfoil chord to give a statement of lift per unit span. However, Grace et al.[13,14] showed how this expression could be used in an inverse process to describe the unsteady flow from an empirical measure of the unsteady pressure response. The mathematical statement of this inversion is straightforward and can be written by arranging Eq. (3) as

$$u_2(\omega) = \frac{\Delta p(x_1, \omega)}{2\rho U \sqrt{\left(1 - x_1^*\right)/\left(1 + x_1^*\right)}\, Se(\omega c/2U)} \quad (4)$$

The application of this expression to experimental data has proven to be more complicated than the simple statement might indicate.

Most of the experimental efforts to date attempting to characterize the unsteady response of a propeller blade or wing have been done at the model scale. At this scale, measurement of the unsteady pressure jump is difficult, and it is typical that the pressure is measured only on a single side of the blade. Therefore, an instantaneous measure of the pressure jump is not available. The pressure jump is antisymmetric for the flat plate, but it is asymmetric for any real airfoil geometry of practical interest. In spite of this, if the airfoil is assumed thin, the flat plate antisymmetry can be used so that the single-sided measurement can be treated to infer the unsteady velocity. Thus, Eq. (4) becomes

$$u_2(\omega) = \frac{p(x_1, \omega)}{\rho U \sqrt{\left(1 - x_1^*\right)/\left(1 + x_1^*\right)}\, Se(\omega c/2U)} \quad (5)$$

In Ref. 8, the authors explored the unsteady pressure distribution as measured on a thin airfoil that closely approximated a flat plate. The results were somewhat unsatisfying to the Sears treatment. It was found that the unsteady pressure distribution was not antisymmetric even for the simple airfoil geometry. Additionally, the values for unsteady pressure aft of the midchord did not correlate to the Sears prediction. In that case, further investigation by Lynch et al.[15] showed that the unsteady pressure distribution was very dependent on viscous effects produced by leading-edge geometry.

The results of these and other experimental efforts by Commerford and Karta,[16] Fujita and Kovasnay,[17] and Fleeter et al.[18] showed the response of the blade would not be modeled well by Eq. (5) for the general case. In particular from the previous experiments, unsteady pressures measured on the pressure and suction faces of the loaded blade were expected to show response differences. In Fig. 19, the unsteady pressure spectra measured at the same radial and chordwise location on opposite sides of different blades are shown for the propeller operating at $J = 1.2$ (3000 rpm) downstream of the 7.6-cm grid. The two pressure spectra are compared to a pressure measurement made on the pressure face of the blade with the propeller operating in clean flow. The spectra show the effect of turbulence ingestion on the measured pressure and the anticipated discrepancy between pressure and suction faces with the suction face levels elevated well above the pressure face levels.

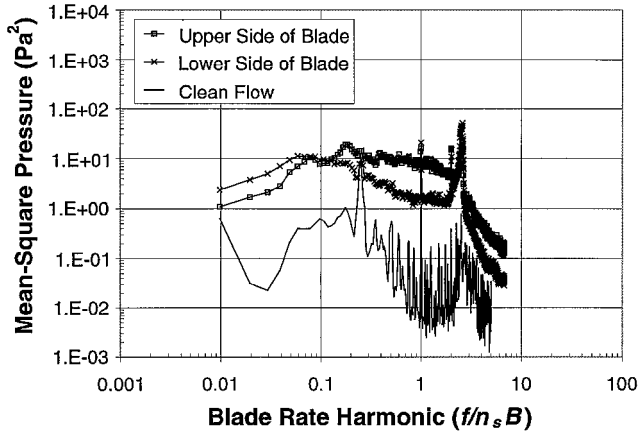

Fig. 19 Broadband pressures measured on the blade faces for the propeller operating at $J = 1.2$ downstream of the 7.6-cm (3-in.) turbulence grid and clean flow.

All three spectra show a large resonance from approximately twice to three times the blade rate frequency. Additional measurements with an accelerometer placed in the hub of the propeller showed a vibration mode in this frequency range, and the resonance observed in the pressure data was attributed to vibration contamination of the signals. Based on the accelerometer data, it was possible to suppress some of the vibration noise over parts of the sensor measurement range for the turbulent flow case. However, for the frequencies at or near the vibration mode, it was not possible to suppress the corrupting vibration noise completely. Therefore, in further presentation of the data, this range will be omitted because the results show effects other than the pressure response of the blade to the incoming turbulence.

When the observed asymmetry and the vibration contamination were kept in mind, an inversion of the pressure data was attempted using Eq. (5) in a form appropriate to application to spectral data,

$$\Phi_u\left(k_1^*\right) = \frac{\Phi_p\left(x_1^*, k_1^*\right)}{\rho^2 U_\infty^2 \left[\left(1 - x_1^*\right)/\left(1 + x_1^*\right)\right] \left|Se\left(k_1^*\right)\right|^2} \quad (6)$$

Thus, an analytical solution of the inverse aerodynamic problem is established relying on the assumptions of a simple geometry, no distortion of the inviscid mean flow by the blade, and no blade-to-blade cascade effects. For the propeller blade, these assumptions will not always hold. Therefore, Eq. (4) can be rewritten to resemble a transfer function between pressure and velocity as

$$\frac{\Phi_p\left(x_1^*, k_1^*\right)}{\Phi_u\left(k_1^*\right)} = \rho^2 U_\infty^2 \left(\frac{1 - x_1^*}{1 + x_1^*}\right) \left|Se\left(k_1^*\right)\right|^2 \quad (7)$$

where the terms found by Sears make up the transfer function. In this form, any of a number of analytical or numerical treatments of aerodynamic admittance can be used to form the transfer function between unsteady pressure and velocity. Alternatively, the function can be estimated empirically by exposing the propeller to known distortions at specific frequencies and measuring the response.

Figure 20 shows the results of the inversion based upon the Sears function for the data shown in Fig. 19. The inferred velocity spectra are plotted against a velocity spectrum measured using the hot-wire anemometer mounted on the rotating blade. Mounting the anemometer on the blade allowed measurement of the turbulent field in the rotating reference frame. However, comparison of measurements made in the two frames showed the spectral form of the turbulence to be invariant when the relative velocity and Taylor's hypothesis were used to estimate the convective wavelength of the turbulence from the measured frequency. In Fig. 20, the wave number of the turbulence has been normalized by the mesh size of the turbulent grid and the velocity spectra have been normalized by the square of the freestream velocity. The inversion indicates that using the Sears response is adequate for characterizing the PS response of the blade. Over much of the measurement range, the assumed Sears

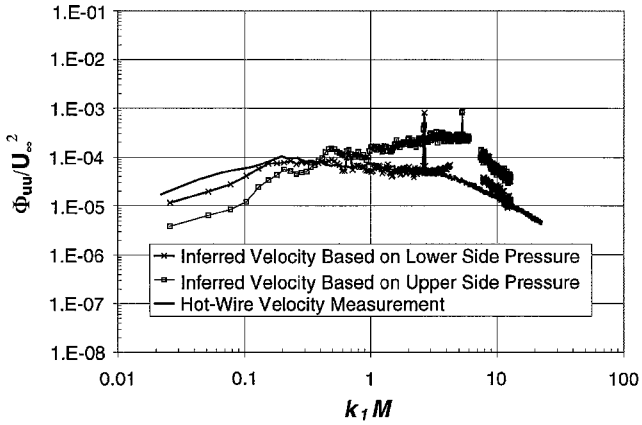

Fig. 20 Comparison of velocity spectrum of grid turbulence measured using hot wire in rotating frame and inferred spectra based on unsteady pressure measured on the blade faces and the sears aerodynamic response function.

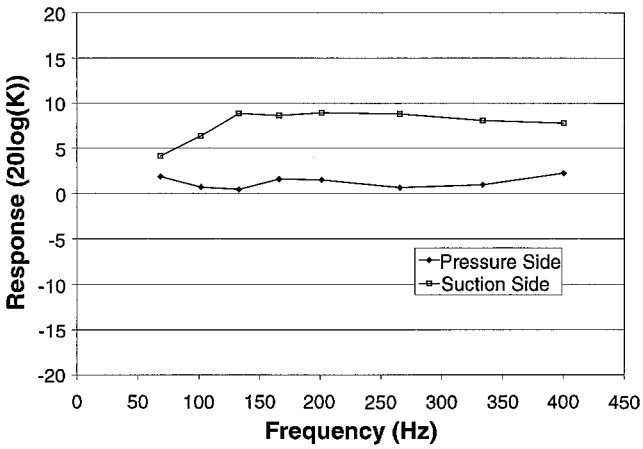

Fig. 21 Comparison between the Sears aerodynamic response function (i.e., zero value) and the response functions measured empirically on each of the blade faces.

response has recovered the correct unsteady velocity spectrum. Near the large vibration mode identified earlier, less agreement is obtained between the measured and inferred spectra (likely due to vibration effects at these frequencies).

The SS spectrum level was observed earlier to be much higher than the PS. Therefore, the velocity spectrum estimated by the Sears function has appropriately high values. To address this issue, the aerodynamic admittance for the unsteady pressure on the suction face was estimated empirically using the cyclic flow devices. Thus, the empirically defined response could be used in Eq. (7) to repeat the inversion process for the suction face. The calibrated response was calculated by modifying Eq. (7) to be

$$\left|K\left(x_1^*, k_1^*\right)\right|^2 = \frac{\Phi_p\left(x_1^*, k_1^*\right)}{\Phi_u\left(k_1^*\right)}\left[1 \Big/ \rho^2 U_\infty^2 \left(\frac{1-x_1^*}{1+x_1^*}\right)\left|Se\left(k_1^*\right)\right|^2\right] \tag{8}$$

Under this definition, if the Sears analysis is appropriate for characterizing the blade response, the empirically defined value of $K(x_1^*, k_1^*)$ would be unity. Variations from unity could then be used to correct empirically the inversion attempted using the flat plate analysis. Therefore, by operating the propeller behind the four-cycle screen and varying the shaft speed of the propeller for a given advance ratio, the unsteady pressure response to the known flow condition was mapped for a range of frequencies. In Fig. 21, the measured blade responses for both sides of the blade are compared. Consistent with the earlier presented data, the PS response is well characterized by the Sears development. However, the SS response is much higher, indicating that the simple flat-plate analysis is not

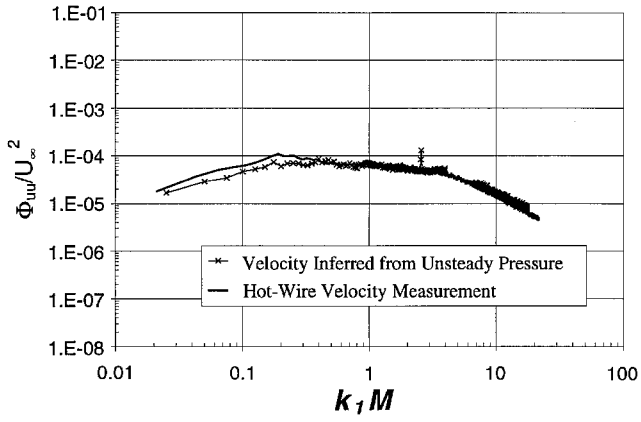

Fig. 22 Comparison of velocity spectrum of grid turbulence measured using hot wire in rotating frame and inferred spectra based on unsteady pressure.

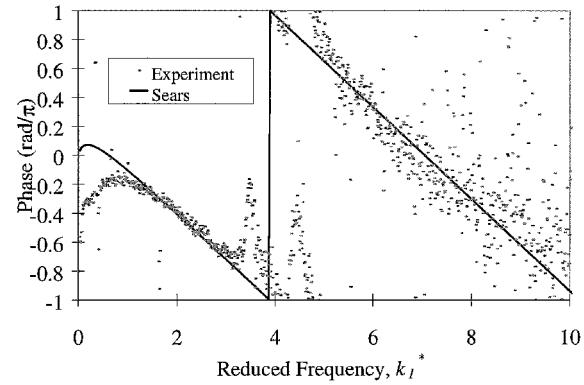

Fig. 23 Relative phase measured between the unsteady pressure and the incoming turbulence compared the phase of the Sears response function.

an appropriate model. Figure 22 shows the results of the inversion based on the empirical response for the suction face pressure. Much better agreement is seen between the inferred and measured spectra relative to the data shown in Fig. 20.

The developments given by Sears and other researchers predict a frequency-dependent variation in phase between the incident velocity gust and the blade response that is almost linear at reduced frequencies above unity. Figure 23 shows a comparison between the experimentally measured phase between velocity and pressure and that given by the Sears function. The data in Fig. 23 are from the suction face of one of the blades. However, the measurement for both faces was nearly identical except for a π phase shift. This showed that, whereas the distribution of the pressure response to gusting seems to be greatly affected by loading and separation, the unsteady phase is not.

In Ref. 1, the low-frequency radiation of a free running propeller ingesting unsteady flow was related to unsteady thrust by

$$\Phi_P(\boldsymbol{r}, \omega) = |G_{PT}(\boldsymbol{r}, \omega)|^2 \Phi_T(\omega) \tag{9}$$

Furthermore, when it is assumed that the thrust could be related to the loading on a single propeller blade by use of a blade-summation gain function, the radiated noise was related to the unsteady blade lift by

$$\Phi_P(\boldsymbol{r}, \omega) \approx |G_{PT}(\boldsymbol{r}, \omega)|^2 |\beta^0(\omega)|^2 (\eta(\bar{\gamma}))^2 \Phi_L(\omega) \tag{10}$$

In practical applications, the complex Green's function given by $G_{PT}(\boldsymbol{r}, \omega)$ may be very difficult to describe. However, for the simpler case presented here, this function is well described by the

free-field dipole Green's function relating far-field radiation to any near-field unsteady force term. This function is given as

$$\Phi_P(\boldsymbol{r}, \omega) = |G_{PT}(\boldsymbol{r}, \omega)|^2 \Phi_T(\omega) \approx \left| \frac{\omega e^{ik_0|\boldsymbol{r}|}}{4\pi|\boldsymbol{r}|c_0} \cos\theta \right|^2 \Phi_T(\omega) \quad (11)$$

where $k_0 = \omega/c_0$ is the acoustic wave number and θ is the observation angle measured from the propeller axis of rotation.

To test the methods ability to characterize the unsteady thrust, a numerical analysis of the propeller response was completed using the techniques of Ref. 1. In particular, the unsteady blade loading was estimated by use of the spanwise strip-theory algorithm for turbulent loading outline based on the measured velocity spectrum, the spanwise integral length scale, and the Sears lift response. This estimate of unsteady blade loading was then coupled with the blade-summation-gain function estimated by use of the blade-pressure-summation technique. From this estimate of unsteady thrust, the acoustic radiation of the propeller was predicted for the loaded propeller operating at $J = 1.2$ (3000 rpm) downstream of the 7.6-cm (3.0-in.) grid in accordance with Eq. (9).

The estimated blade-summation gain is shown in Fig. 24. Over most of the frequency range, it is approximately the zero coherence value B. However, for small ranges near and to the right of the blade rate harmonics, some increased summation gain is observed in accordance with Martinez.[19–21] Note that the summation gain at twice the BPF is much smaller than that near the BPF and is dominated by a blade passage tone. The results are likely due to remnants of the grid geometry pattern in the mean flowfield that were found using the hot-wire anemometer.

Based on the measured summation gain, the unsteady thrust was estimated from the blade lift and, assuming dipole radiation, the

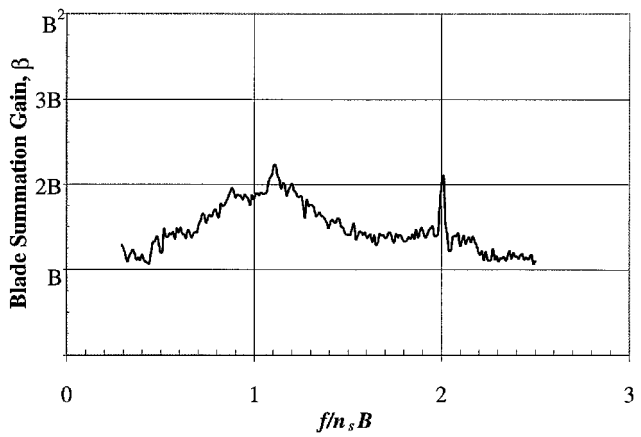

Fig. 24 Array gain measured by the coherent sum of unsteady pressures measured on the blades of propeller operating at $J = 1.2$ downstream of the 7.6-cm (3-in.) turbulence grid showing force enhancement near the blade rate harmonics with shift to higher frequency.

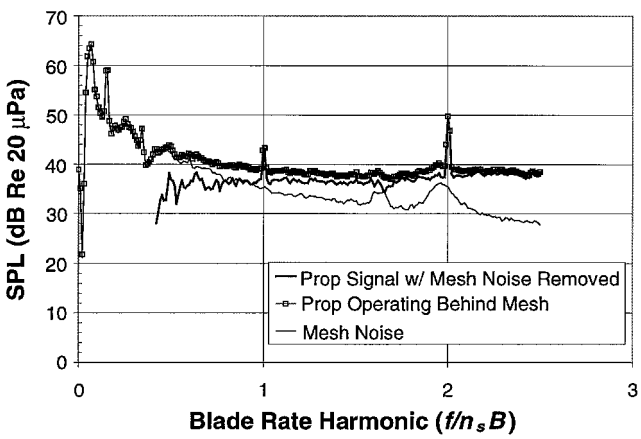

Fig. 25 Radiated noise measured at off-axis location for the propeller operating at $J = 1.2$ downstream of the 7.6-cm (3-in.) turbulence grid compared to noise of grid.

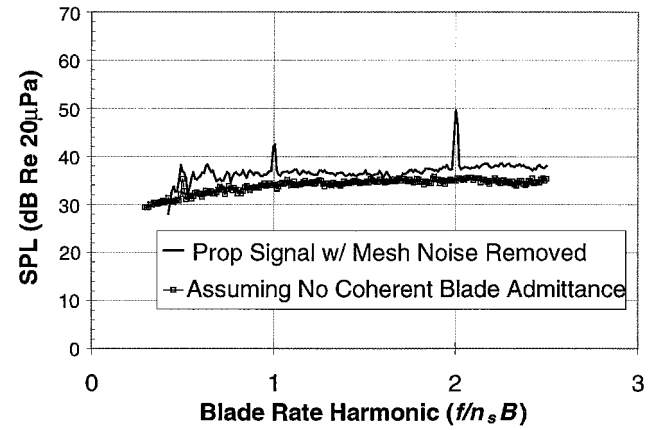

Fig. 26 Comparison between measured radiated signature and predicted noise from two-dimensional strip theory analysis of propeller operating at $J = 1.2$ downstream of the 7.6-cm (3-in.) turbulence grid for incoherent gain.

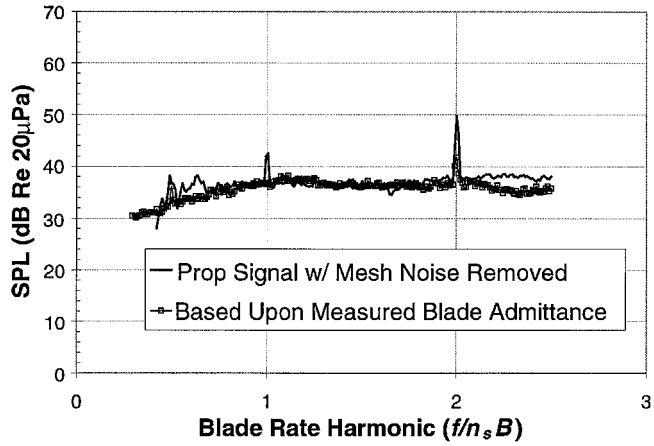

Fig. 27 Comparison between measured radiated signature and predicted noise using two-dimensional strip theory analysis of propeller operating at $J = 1.2$ downstream of the 7.6-cm (3-in.) turbulence grid for measured array gain.

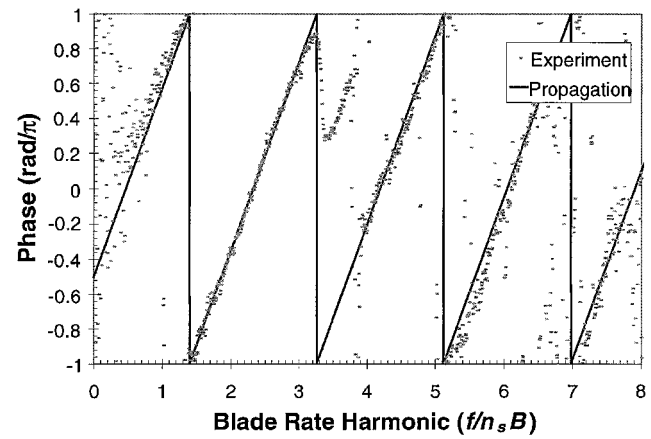

Fig. 28 Measured phase between pressure near and far fields compared to a direct dipole phase model.

SPL spectrum was predicted for a single point in the acoustic field using the unsteady thrust as a dipole source. The computation was then compared to an experimental measurement obtained using a B&K microphone, shown in Fig. 25. Figures 26 and 27 show the comparison between the measured spectrum and predictions made with the measured blade-summation gain and the zero-coherence-summation gain B. Both computations are in approximate agreement with the experimental data. However, the prediction using

the zero-coherence value consistently underpredicted the measured value. The prediction based on the measured blade summation showed better agreement, although the value was high for some frequencies.

Finally, assuming the acoustic pressure in the far field was a propagating wave, the relative phase between the unsteady thrust and the acoustic radiation was estimated. In the current experimental configuration, no means of directly measuring the unsteady thrust existed. Therefore, the unsteady thrust was approximated using the sum of the ring array output. Figure 28 shows a comparison between the predicted and measured relative phase between the summed pressure and the acoustic measurement. Excellent agreement is observed over most of the frequency range except in the region of vibration as identified earlier. This further confirms the use of the ring array sum to approximate the blade-summation gain and characterize unsteady thrust.

Conclusions

Interpreting the near-field pressure response of rotating machinery is convenient for use in identifying and quantifying sources of acoustic noise. The techniques developed in Ref. 1 and here are primarily oriented toward the analysis of the blade response associated with leading-edge interaction with ingested unsteady flow. For this problem, the near-field pressure response was related to both the incoming flowfield and the radiated acoustic field. Thus, characteristics of the flow were associated with particular sources, such as unsteady thrust or side force, and used to predict the radiated signature. The agreement between the measured and predicted signatures indicates that the physics governing the propagation from near to far field are well understood. However, empirical characterization of the near-field response in a manner relevant to relating the unsteady flow quantities to the radiated field is still necessary.

In the current experimental effort, flowfields composed primarily of large-scale, mean-flow distortions with axisymmetric patterns were used to demonstrate the use of the blade-summation technique. In these cases, by varying the rotational speed of the propeller, the individual blade response was mapped over a range of frequency giving an empirical measure of the relation between velocity and pressure. The unsteady thrust, side force, and the resulting acoustic radiation based on the summation gain showed excellent agreement with a measurement of the acoustic radiation. Extending the results to the general case, the methods were applied to the propeller ingesting grid-generated, small-scale turbulence. In this case, the individual blade response was interpreted using the classical thin airfoil techniques as well as using the empirical definitions obtained in the cyclic flow cases. Again, the total response was predicted using the empirical summation gain and compared favorably to the measured acoustic radiation.

Acknowledgments

This research was performed at the Hessert Center for Aerospace Research, Department of Aerospace and Mechanical Engineering, University of Notre Dame, for the U.S. Navy, Office of Naval Research, Arlington, Virginia, under Contracts N00014-95-1-0488 and N00014-97-0489 and Subcontract N00167-402.15-UND with Cambridge Acoustical Associates, Inc. The authors would like to thank the Program Manager, Lawrence P. Purtell.

References

[1]Minniti, R. J., Blake, W. K., and Mueller, T. J., "Inferring Propeller Inflow and Radiation from Near-Field Response, Part 1: Analytic Development," *AIAA Journal*, Vol. 39, No. 6, 2000, pp. 1030–1036.

[2]Mueller, T. J., Scharpf, D. F., Batill, S. M., Strebinger, R. B., Sullivan, C. J., and Subramanian, S., "The Design of a Low-Noise, Low-Turbulence Wind Tunnel for Acoustic Measurements," AIAA Paper 92-3883, 1992.

[3]Mueller, T. J., Scharpf, D. F., Batill, S. M., Strebinger, R. B., Sullivan, C. J., and Subramanian, S., "A New Low Speed Wind Tunnel for Acoustic Measurements," *European Forum on Wind Tunnels and Wind Tunnel Test Techniques*, Royal Aeronautical Society, London, 1992, pp. 6.1–6.13.

[4]Minniti, R. J., Batill, S. M., and Mueller, T. J., "Experimental Uncertainty of Sound Pressure Level Measurements Made in a Free-Jet Anechoic Wind Tunnel Facility," *First Joint CEAS/AIAA Aeroacoustics Conference*, Vol. 2, 1995, pp. 1105–1114.

[5]Scharpf, D. F., "An Experimental Investigation of the Sources of Propeller Noise Due to Turbulence Ingestion," Ph.D. Dissertation, Univ. of Notre Dame, Notre Dame, IN, Jan. 1993.

[6]Minniti, R. J., III, "An Experimental Investigation of Thin Airfoils Exposed to Periodic Gusting Including the Inverse Aeroacoustic Problem," Ph.D. Dissertation, Univ. of Notre Dame, Notre Dame, IN, April 1997.

[7]Minniti, R. J., III, Sullivan, C. J., and Mueller, T. J., "A Thin Film Sensor for the Measurement of Unsteady Pressure," *Aeronautical Journal of the Royal Aeronautical Society*, No. 2311, Aug./Sept. 1998, pp. 393–398.

[8]Minniti, R. J., III, and Mueller, T. J., "Experimental Investigation of Unsteady Aerodynamics and Aeroacoustics of a Thin Airfoil," *AIAA Journal*, Vol. 36, No. 7, 1998, pp. 1149–1156.

[9]Lynch, D. L., Minniti, R. J., and Mueller, T. J., "The Influence of Leading Edge Separation on the Unsteady Response of a Thin Airfoil," *Proceedings of the ASME, Noise Control and Acoustics Division*, NCA-Vol. 25, American Society of Mechanical Engineers, Fairfield, NJ, 1998, pp. 57–65.

[10]Sullivan, C. J., "Design and Development of Experimental Techniques for the Measurement of Unsteady Pressure on Propeller Blades with Piezoelectric Film," Ph.D. Dissertation, Univ. of Notre Dame, Notre Dame, IN, Dec. 1996.

[11]Subramanian, S., and Mueller, T. J., "An Experimental Study of Propeller Noise Due to Cyclic Flow Distortions," *Journal of Sound and Vibration*, Vol. 183, No. 5, 1995, pp. 907–923.

[12]Scharpf, D. F., and Mueller, T. J., "An Experimental Investigation of the Sources of Propeller Noise Due to the Investigation of Turbulence at Low Speeds," *Experiments in Fluids*, Vol. 18, No. 4, 1995, pp. 277–287.

[13]Grace, S. M., Atassi, H. M., and Blake, W. K., "Inverse Aeroacoustic Problem for a Streamlined Body Part 1: Basic Formulation," *AIAA Journal*, Vol. 34, No. 11, 1996, pp. 2233–2240.

[14]Grace, S. M., Atassi, H. M., and Blake, W. K., "Inverse Aeroacoustic Problem for a Streamlined Body Part 2: Numerical Accuracy," *AIAA Journal*, Vol. 34, No. 11, 1996, pp. 2241–2246.

[15]Lynch, D. A., III, Minniti, R. J., III, and Mueller, T. J., "The Influence of Leading Edge Separation on the Unsteady Response of a Thin Airfoil," *Proceedings of the IMECE'98*, American Society of Mechanical Engineers, Fairfield, NJ, 1998, pp. 1–9.

[16]Commerford, G. L., and Karta, F. O., "Unsteady Aerodynamic Response of a Two-Dimensional Airfoil at High Reduced Frequency," *AIAA Journal*, Vol. 12, No. 1, 1974, pp. 44–48.

[17]Fujita, H., and Kovasznay, S. G., "Unsteady Lift and Radiated Sound from a Wake Cutting Airfoil," *AIAA Journal*, Vol. 12, No. 9, 1974, pp. 1216–1221.

[18]Fleeter, S., Capece, V. R., and Chiang, H.-W. D. "Unsteady Aerodynamic Gust Response Including Steady Flow Separation," *AIAA Journal*, Vol. 26, No. 6, 1990, pp. 1024–1031.

[19]Martinez, R., "Broadband Sources of Structure-Borne Noise for Propulsors in 'Haystacked' Turbulence," *Computers and Structures*, Vol. 65, No. 30, 1995, pp. 475–490.

[20]Martinez, R., "Asymptotic Theory of Broadband Rotor Thrust, Part 1: Manipulations of Flow Probabilities for a High Number of Blades," *Journal of Applied Mechanics*, Vol. 63, March 1996, pp. 136–142.

[21]Martinez, R., "Asymptotic Theory of Broadband Rotor Thrust, Part 2: Analysis of the Right Frequency Shift of the Maximum Response," *Journal of Applied Mechanics*, Vol. 63, March 1996, pp. 143–148.

P. J. Morris
Associate Editor